CERN-ATS-Note-2011-016 PERF
BCNWG Note 2

LHC BUNCH CURRENT NORMALIZATION FOR THE OCTOBER 2010 LUMINOSITY CALIBRATION MEASUREMENTS

A. Alici[1], G. Anders[2,3], N. Bacchetta[3], V. Balagura[3,5], C. Barschel[3,6], D. Belohrad[3], D. Berge[3], F. Bossù[4,8], H. Burkhardt[3], S.I. Cooper[7], M. Ferro-Luzzi[3], G. Franzoni[7], C. Gabaldon[3], M. Gagliardi[8], J.J. Gras[3], V. Halyo[9], B. Heinemann[10], P. Hopchev[11], A. Hunt[9], W. Kozanecki[12], Y. Kubota[7], S. Kwan[13], M. Ludwig[3], D. Marlow[9], P. Odier[3], S. Pagan Griso[10], J. Panman[3], T. Pauly[3], S. Thoulet[3], S. White[3], J.C. Yun [13], and M. Zanetti[14]

[1]Centro Studi e Ricerche e Museo Storico della Fisica “Enrico Fermi”, Rome, Italy and INFN Sezione di Bologna, Italy
[2]Ruprecht-Karls-Universität Heidelberg: Kirchhoff-Institut für Physik, Heidelberg, Germany
[3]CERN, Geneva, Switzerland
[4]Università degli Studi, Torino, Italy
[5]Institute of Theoretical and Experimental Physics (ITEP), Moscow, Russia
[6]RWTH Aachen University, III. Physikalisches Institut A, Aachen, Germany
[7]University of Minnesota, Minneapolis, USA
[8]INFN sezione di Torino, Torino, Italy
[9]Princeton University, Princeton, New Jersey, USA
[10]Lawrence Berkeley National Laboratory and University of California, Berkeley, California, USA
[11]LAPP Annecy, France
[12]CEA, DSM/IRFU, Centre d’Etudes de Saclay, FR - 91191 Gif-sur-Yvette, France
[13]Fermi National Accelerator Laboratory, Batavia, Illinois, USA
[14]Massachusetts Institute of Technology, Cambridge, Massachusetts, USA

October 20, 2011

Abstract

In October 2010, a second series of luminosity calibration measurements was performed for each LHC Interaction Point at the zero-momentum frame energy $\sqrt{s} = 7$ TeV. In this note, the results are presented of the LHC bunch current normalization analysis for these experiments. The uncertainties, and the prospects to reduce these for future experiments, are discussed in detail.

Contents

1 Introduction

A first series of luminosity calibration experiments was carried out in April-May 2010 to obtain physics cross section normalizations at each Interaction Point (IP) at the zero-momentum frame energy $\sqrt{s} = 7$ TeV [2, 1]. From these measurements, it resulted that the total uncertainties were dominated by the bunch current normalization. As a consequence, a detailed bunch population analysis was carried out using data from the LHC Beam Current Transformers (BCTs) and from the experiments. An analysis procedure was defined and bunch poupulation uncertainties quantified. The analysis and results were documented in a first bunch current normalization note [3]. We refer the reader to this document for a detailed description of the procedure used to determine the bunch populations and their associated uncertainties. A second series of luminosity calibration experiments was carried out in October 2010. The bunch current normalization for these October measurements is the subject of the present note.

The method used for the bunch population normalization is largely the same as was used for the detailed analysis of the April-May 2010 scans. A few differences between the first and second series may be noted. In October 2010, higher bunch and beam intensities were used. This results in a reduction of several relative uncertainties, as will be shown in this note. A minor novelty in the procedure used here is the treatment of the ghost charge fraction and its uncertainty. In the April-May analysis, a correction of the total current was applied, when necessary, to take into account the amount of ghost charge. The uncertainty associated with this correction was neglected. For the Ocober scans, given the reduction of several (relative) contributions to the bunch populations uncertainties, an estimate of the ghost charge uncertainty is taken into account.

The rest of this note is organized as follows. In section 2 the October 2010 van der Meer scan measurements are outlined. Section 3 presents the results of the bunch population data analysis. Section 4 concludes this work with a discussion and summary.

2 The October 2010 van der Meer scans

The October 2010 van der Meer scans took place in a period when the LHC was being operated with 150 ns bunch trains. The same optics and crossing scheme were used as during luminosity production. All IP optics were squeezed to $\beta^* = 3.5$ m (as opposed to $\beta^* = 2$ m in April-May 2010). A 100 μrad (110 μrad) external crossing half-angle was present at IP1&5 and IP8 (IP2) . This resulted in a net crossing half-angle ϕ of 100, 240 and 70 μrad at IP1&5, IP2 and IP8.

Fill 1386, 1 October 2010, 19-bunch pattern, $\sim 9 \cdot 10^{10}$ p/bunch			
Scan	Period label	Start time	Stop time
X Scan IP1	A1	13 : 50	14 : 02
Y Scan IP1	A2	14 : 07	14 : 19
X Scan IP1	A3	14 : 23	14 : 38
Y Scan IP1	A4	14 : 40	14 : 54
X Scan IP1 with offset $\Delta_y \approx 60\mu m$	A5	14 : 58	15 : 06
Y Scan IP1 with offset $\Delta_x \approx 60\mu m$	A6	15 : 08	15 : 17
X Scan IP5	C1	15 : 32	15 : 44
Y Scan IP5	C2	15 : 49	16 : 05
X Scan IP5 moved Beam1 only	C3	16 : 05	16 : 18

Table 1: Separation scans performed during fill 1386 for ATLAS and CMS. The (approximate) start/stop times are Geneva local time.

The van der Meer scans took place in two dedicated LHC fills, namely fills 1386 and 1422. The most important change, with respect to the April-May scans, was the use of higher beam and bunch intensities. The normalized transverse emittance was about nominal (3.75 μm). Table 1 shows the different periods where the van der Meer scans have been performed for ATLAS (A1, A2, A3, A4, A5, A6) and CMS (C1, C2, C3, C4) in fill 1386. Table 2 shows the same information for the scans performed for LHCb (B1, B2, B3, B4), CMS (C1, C2, C3, C4) and ALICE (AL1, AL2, AL3, AL4) in fill 1422.

The bunch patterns used during these experiments were either with 19 bunches per beam (fill 1386) or with 16 bunches per beam (fill 1422). In these patterns each bunch was colliding with exactly one bunch from

Fill 1422, 15 October 2010, 16-bunch pattern, $\sim 7.5 \cdot 10^{10}$ p/bunch			
Scan	Period label	Start time	Stop time
X Scan IP8	B1	13 : 43	14 : 02
Y Scan IP8	B2	14 : 03	14 : 22
X Scan IP8 moved single beam	B3	14 : 25	14 : 40
Y Scan IP8 moved single beam	B4	14 : 44	14 : 58
X Scan IP5 moved Beam1 only	C1	15 : 19	15 : 33
Y Scan IP5 moved Beam1 only	C2	15 : 34	15 : 47
X Scan IP5 moved Beam2 only	C3	15 : 47	16 : 03
Y Scan IP5 moved Beam2 only	C4	16 : 04	16 : 16
X Scan IP2	AL1	16 : 32	16 : 53
Y Scan IP2	AL2	16 : 53	17 : 11
X Scan IP2 reversed direction	AL3	17 : 16	17 : 33
Y Scan IP2 reversed direction	AL4	17 : 33	17 : 51

Table 2: Separation scans performed during fill 1422 for LHCb, ALICE and CMS. The (approximate) start/stop times are Geneva local time.

Fill 1386: 19-bunch pattern							
Beam1		Colliding Beam2 RF bucket				Beam2	
bunch nr	RF bucket	IP1	IP2	IP5	IP8	bunch nr	RF bucket
1	1	1	-	1	-	1	1
2	5001	5001	-	5001	-	2	501
3	8611	8611	-	8611	-	3	1501
4	9441	-	-	-	501	4	2501
5	10441	-	-	-	1501	5	3501
6	11441	-	-	-	2501	6	5001
7	12441	-	-	-	3501	7	8611
8	14501	14501	-	14501	-	8	10111
9	16501	16501	-	16501	-	9	11111
10	17201	-	26111	-	-	10	12111
11	19051	-	-	-	10111	11	13111
12	20051	-	-	-	11111	12	14501
13	21051	-	-	-	12111	13	16501
14	22051	-	-	-	13111	14	18791
15	23001	23001	-	23001	-	15	19791
16	27731	-	-	-	18791	16	20791
17	28731	-	-	-	19791	17	21791
18	29731	-	-	-	20791	18	23001
19	30731	-	-	-	21791	19	26111

Table 3: List of bunch crossings in the four insertion regions for the 19-bunch pattern used in fill 1386. In each line the RF bucket of the encountered Beam2 bunch is given for each IP and for the corresponding bucket of the Beam1 bunch.

the other beam, i.e. only in IP2 or in IP8 or in IP1 and IP5 (by symmetry, all bunch pairs which cross at IP1 cross as well at IP5). The nominally filled RF buckets* are given in tables 3 and 4, along with the collision pairing.

In the October scans, the beam currents were $1.7 \cdot 10^{12}$ p in fill 1386 and $1.2 \cdot 10^{12}$ p in fill 1422. Given these beam intensities, Range 3 of the DCCT systems was used, which is characterized by a nominal scaling factor of 10^{12} elementary charges per Volt, a full scale of $5 \cdot 10^{12}$ elementary charges and a least-significant bit equivalent to $2.44 \cdot 10^{9}$ elementary charges.

*The LHC contains 35640 RF buckets spaced by about 2.5 ns, conventionally numbered from 1 to 35640 and here phased such that bucket 1 of both beams collided in IP1 and IP5.

Fill 1422: 16-bunch pattern							
Beam1		Colliding Beam2 RF bucket				Beam2	
bunch nr	RF bucket	IP1	IP2	IP5	IP8	bunch nr	RF bucket
1	1	1	-	1	-	1	1
2	501	5001	-	5001	-	2	501
3	1001	1001	-	1001	-	3	1001
4	20261	-	-	-	11321	4	2411
5	20761	-	-	-	11821	5	11321
6	21261	-	-	-	12321	6	11821
7	21761	-	-	-	12821	7	12321
8	22361	-	-	-	13421	8	12821
9	22861	-	-	-	13921	9	13421
10	23361	-	-	-	14421	10	13921
11	23861	-	-	-	14921	11	14421
12	24461	-	-	-	15521	12	14921
13	24961	-	-	-	16021	13	15521
14	25461	-	-	-	16521	14	16021
15	25961	-	-	-	17021	15	16521
16	29141	-	2411	-	-	16	17021

Table 4: List of bunch crossings in the four insertion regions for the 16-bunch pattern used in fill 1422. In each line the RF bucket of the encountered Beam2 bunch is given for each IP and for the corresponding bucket of the Beam1 bunch.

In the April-May experiments, the main contribution to the total uncertainty stemmed from DCCT baseline offset variations Since this effect does not scale proportionally with beam and bunch intensity, the DCCT measurement uncertainties were much reduced in October relative to the April-May measurements.

3 Bunch population data analysis

As discussed in reference [3], the DCCT measurements are used to normalize the sum of the individual bunch populations, after correcting for a possible amount of ghost charge $N_{\rm ghost}$. Explicitly, the total beam population $N_{\rm tot}$ and the individual bunch populations N_i ($i = 1, ...n$ running over all nominally filled bunch slots) are given by

$$N_{\rm tot} = \alpha \cdot S_{\rm DCCT} \ , \qquad N_i = a S_i \ , \qquad a = \frac{N_{\rm tot} - N_{\rm ghost}}{\sum\limits_{i=1}^{n} S_i} = \frac{N_{\rm tot}}{\sum\limits_{i=1}^{n} S_i} (1 - f_{\rm ghost}) \tag{1}$$

where α is the calibrated absolute scale factor of the DCCT (elementary charges/V), $S_{\rm DCCT}$ the signal measured by the DCCT (V) after correcting for the baseline offset, and the S_i's are the individual bunch signals measured by the FBCT.

As for the April-May 2010 scans, the amount of ghost charge was estimated from detector data.

Note that, for the sake of conciseness, the total beam and single bunch population values presented below are averages over the full van der Meer scan period, in each fill (i.e. from 13:50 to 16:18 for fill 1386 and 13:43 to 17:51 for fill 1422). More adequate average values over a specific (shorter) period of circulating beam can be obtained by averaging the BCT data over this period.

3.1 Total beam populations

Figure 1 shows the system A and B DCCT measurements for both beams and for the two relevant LHC fills. The results for the averaged intensity before, during and after each van der Meer scan fill are summarized in table 5 for system A and table 6 for system B. The measurement uncertainties are peak-to-peak bounds

$\pm\Delta N_{\mathrm{tot}}$, as defined in reference [3]. The last column shows the intensities, averaged over the time period covering all scans (as defined in tables 1 and 2). The DCCT measurements of the beam intensities showed a decay of the order of 1-2% during the whole periods considered here. Conservatively, a fixed peak-to-peak bound of $\pm 0.81 \cdot 10^9$ is assigned to all resulting intensity values. Contrary to the April-May measurements, the DCCT baseline offset correction is here negligible (less than 0.1%).

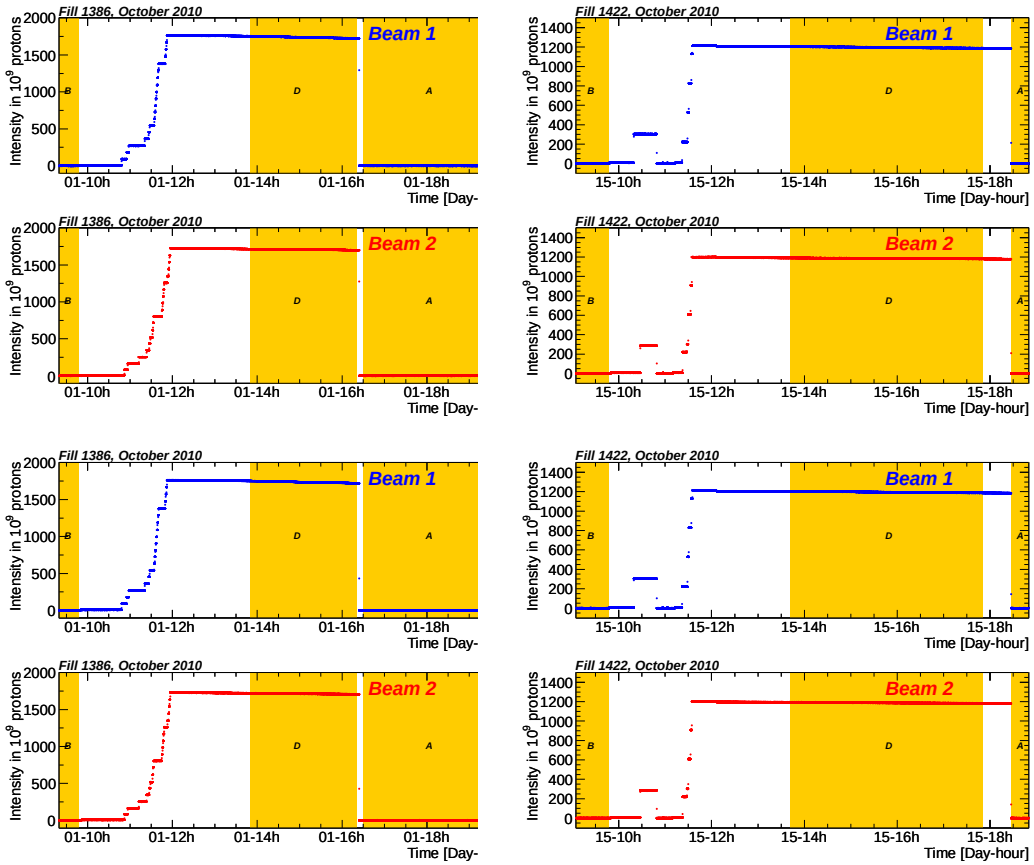

Figure 1: DCCT measurements. Left: fill 1386. Right: fill 1422. From top to bottom: Beam1 system A, Beam2 system A, Beam1 system B, Beam2 system B. The periods “before”, “during” and “after” the scans used to determine the beam currents are indicated by the shaded bands B, D and A.

Fill nr.	LHC ring j	DCCT intensity $\alpha S_{\mathrm{DCCT}} \cdot 10^{-9}$ Before	During	After	LHC intensity $N_{\mathrm{tot},j} \cdot 10^{-9}$ baseline-corrected
1386	1	-0.02 ± 0.57	1738.02	-0.05 ± 0.81	1738.06 ± 0.81
	2	-0.47 ± 0.18	1707.99	-0.56 ± 0.55	1708.52 ± 0.55
1422	1	-0.43 ± 0.30	1196.38	-0.08 ± 0.37	1196.49 ± 0.37
	2	$+0.11 \pm 0.26$	1186.60	-0.23 ± 0.22	1186.82 ± 0.26

Table 5: DCCT System A total population measurements for the October 2010 fills with van der Meer scans (given in 10^9 protons). The uncertainties quoted here for beam j are peak-to-peak bounds $\pm\Delta N_{\mathrm{tot},j}$.

As for the April-May scans, an unweighted average of the two systems (A and B) is taken for the total offset-corrected currents. These average values are listed in table 7. The differences between the results of system A and B range from 0.1 to 1.7%, which is within the estimated scale factor uncertainty ($\Delta\alpha/\alpha = \pm 2\%$).

Given the much improved relative accuracy of the DCCT measurements during the October scans (as compared to the April-May scans), a comparison of the DCCT current decay with the FBCT summed signals decay is here meaningful. Figure 2 shows this comparison for the two rings and two fills. The system A

Fill nr.	LHC ring j	DCCT intensity $\alpha S_{\mathrm{DCCT}} \cdot 10^{-9}$ Before	During	After	LHC intensity $N_{\mathrm{tot},j} \cdot 10^{-9}$ baseline-corrected
1386	1	$+0.24 \pm 0.23$	1736.46	$+0.39 \pm 0.60$	1736.12 ± 0.6
	2	-0.19 ± 0.25	1713.31	$+0.48 \pm 0.38$	1713.07 ± 0.38
1422	1	$+0.04 \pm 0.28$	1194.93	$+0.15 \pm 0.26$	1194.79 ± 0.28
	2	-0.22 ± 0.19	1187.91	-0.98 ± 0.50	1195.84 ± 0.50

Table 6: DCCT System B total population measurements for the October 2010 fills with van der Meer scans (given in 10^9 protons). The uncertainties quoted here for beam j are peak-to-peak bounds $\pm\Delta N_{\mathrm{tot},j}$.

Fill nr.	LHC ring j	LHC intensity $N_{\mathrm{tot},j} \cdot 10^{-9}$ baseline-corrected
1386	1	1737.10 ± 0.81
	2	1710.80 ± 0.81
1422	1	1195.64 ± 0.81
	2	1191.33 ± 0.81

Table 7: DCCT total population measurements for October fills with van der Meer scans (given in 10^9 protons). The uncertainties quoted here for beam j are peak-to-peak bounds $\pm\Delta N_{\mathrm{tot},j}$ as defined in the text.

FBCT summed values were adjusted to the system A DCCT measurement at the start of the fill. A difference between the FBCT sum and DCCT measurements develops during the fill. However, the agreement stays within 0.2% for fill 1386 and 0.3% for fill 1422.

3.2 Relative bunch populations

Figures 3 and 4 show the individual bunch signals (each normalized to its first data point) from the FBCT system A as a function of time, for both beams and for the two relevant LHC fills. The relative decay of each bunch exhibits a spread and is clearly dependent on the number of collisions. It ranges from 2.7 to 4.8% (Beam1) and from 1.0 to 1.6% (Beam2) in fill 1386, and from 0.5 to 3.0% (Beam1) and from 0.5 to 1.7% (Beam2) in fill 1422.

The FBCT data were again compared to the ATLAS BPTX data, which measures in a totally independent manner the relative bunch populations. Figure 5 shows the BPTX data versus the FBCT data for each fill and each beam. A line fit $N_{i,j}^{BPTX} = p \cdot N_{i,j}^{FBCT} + q$ gives an estimate of the slope p and offset q (for ring j). The results of the fits are:

$$\begin{aligned}
\text{Fill 1386:} \quad & N_{i,1}^{BPTX} = (1.07 \pm 0.20) \cdot N_{i,1}^{FBCT} - (5.64 \pm 0.17) \cdot 10^9 \\
& N_{i,2}^{BPTX} = (1.07 \pm 0.10) \cdot N_{i,2}^{FBCT} - (5.99 \pm 0.09) \cdot 10^9 \\
\text{Fill 1422:} \quad & N_{i,1}^{BPTX} = (1.07 \pm 0.10) \cdot N_{i,1}^{FBCT} - (5.06 \pm 0.07) \cdot 10^9 \\
& N_{i,2}^{BPTX} = (1.07 \pm 0.09) \cdot N_{i,2}^{FBCT} - (5.23 \pm 0.07) \cdot 10^9
\end{aligned} \tag{2}$$

Therefore, it is likely that the differences between the BPTX and FBCT bunch population measurements are primarily caused by a non-proportionality (offset). Here, no attempt is made to determine which of the two systems has an offset with respect to the true bunch population (both could have one).

The populations $N_{i,j}$ are given as fraction (percentage) of the sum of $N_{i,j}$'s, in table 8 for fill 1386 and table 9 for fill 11422. In these tables, by definition, $N_{\mathrm{tot},j} = \sum_{i=1,\ldots n} N_{i,j}^{BPTX} = \sum_{i=1,\ldots n} N_{i,j}^{FBCT} \equiv \sum_{i=1,\ldots n} N_{i,j}$.

Like for the scans in April-May, we estimate (conservatively) the relative bunch population uncertainty from the largest difference between the two systems observed in either ring and in any one of the relevant fills. The maximum relative difference amounts to 1.67%. Conservatively, this value is assigned to $\Delta N_i / N_i$ and the uncertainties between bunch populations within the same fill and same beam are to be considered as fully correlated.

LHC ring j	bunch i	RF Bucket	$\frac{N_{i,j}^{BPTX}}{N_{\mathrm{tot},j}}$ (%)	$\frac{N_{i,j}^{FBCT}}{N_{\mathrm{tot},j}}$ (%)	$\frac{N_{i,j}^{FBCT}-N_{i,j}^{BPTX}}{N_{i,j}^{FBCT}}$ (%)
	1	1	5.10	5.09	−0.05
	2	5001	4.94	4.95	+0.35
	3	8611	4.92	4.95	+0.66
	4	9441	5.51	5.47	−0.74
	5	10441	5.17	5.17	−0.13
	6	11441	5.03	5.04	+0.23
	7	12441	5.25	5.24	−0.20
	8	14501	5.09	5.10	+0.10
	9	16501	4.79	4.81	+0.58
1	10	17201	5.44	5.42	−0.51
	11	19051	5.00	5.03	+0.63
	12	20051	5.37	5.38	+0.08
	13	21051	5.75	5.72	−0.51
	14	22051	5.70	5.67	−0.52
	15	23001	4.91	4.94	+0.56
	16	27731	5.63	5.62	−0.21
	17	28731	5.68	5.66	−0.36
	18	29731	5.28	5.30	+0.33
	19	30731	5.45	5.45	+0.06
	1	1	4.68	4.71	+0.59
	2	501	4.75	4.78	+0.60
	3	1501	5.25	5.21	−0.71
	4	2501	5.31	5.28	−0.59
	5	3501	5.30	5.29	−0.23
	6	5001	4.64	4.67	+0.67
	7	8611	5.76	5.73	−0.63
	8	10111	5.86	5.79	−1.07
	9	11111	4.94	4.99	+0.88
2	10	12111	5.02	5.07	+0.82
	11	13111	5.44	5.45	+0.16
	12	14501	5.16	5.17	+0.09
	13	16501	5.31	5.31	−0.06
	14	18791	5.30	5.31	+0.27
	15	19791	5.15	5.18	+0.57
	16	20791	5.50	5.50	+0.03
	17	21791	5.64	5.62	−0.26
	18	23001	5.29	5.28	−0.23
	19	26111	5.70	5.67	−0.43

Table 8: Relative bunch population measurements with the FBCT and ATLAS BPTX systems averaged over the duration of the van der Meer scans in fill 1386.

LHC ring j	bunch i	RF Bucket	$\frac{N_{i,j}^{BPTX}}{N_{\mathrm{tot},j}}$ (%)	$\frac{N_{i,j}^{FBCT}}{N_{\mathrm{tot},j}}$ (%)	$\frac{N_{i,j}^{FBCT}-N_{i,j}^{BPTX}}{N_{i,j}^{FBCT}}$ (%)
1	1	1	6.48	6.45	−0.47
	2	501	5.84	5.85	+0.28
	3	1001	5.85	5.87	+0.20
	4	20261	7.07	7.01	−0.80
	5	20761	6.63	6.61	−0.23
	6	21261	6.20	6.21	+0.17
	7	21761	5.42	5.48	+1.14
	8	22361	6.07	6.09	+0.20
	9	22861	6.20	6.20	+0.09
	10	23361	5.81	5.84	+0.61
	11	23861	6.51	6.49	−0.17
	12	24461	6.31	6.31	−0.06
	13	24961	6.58	6.56	−0.33
	14	25461	5.76	5.79	+0.60
	15	25961	6.23	6.22	−0.03
	16	29141	7.05	7.00	−0.72
2	1	1	6.57	6.53	−0.67
	2	501	5.93	5.94	+0.15
	3	1001	5.85	5.86	+0.25
	4	2411	6.66	6.60	−0.90
	5	11321	6.72	6.69	−0.41
	6	11821	6.71	6.70	−0.26
	7	12321	6.36	6.36	+0.02
	8	12821	5.89	5.91	+0.41
	9	13421	6.99	6.95	−0.62
	10	13921	6.11	6.13	+0.18
	11	14421	6.06	6.08	+0.23
	12	14921	5.69	5.73	+0.74
	13	15521	6.53	6.52	−0.23
	14	16021	6.52	6.52	+0.01
	15	16521	5.17	5.25	+1.67
	16	17021	6.23	6.24	+0.02

Table 9: Relative bunch population measurements with the FBCT and ATLAS BPTX systems averaged over the duration of the van der Meer scans in fill 1422.

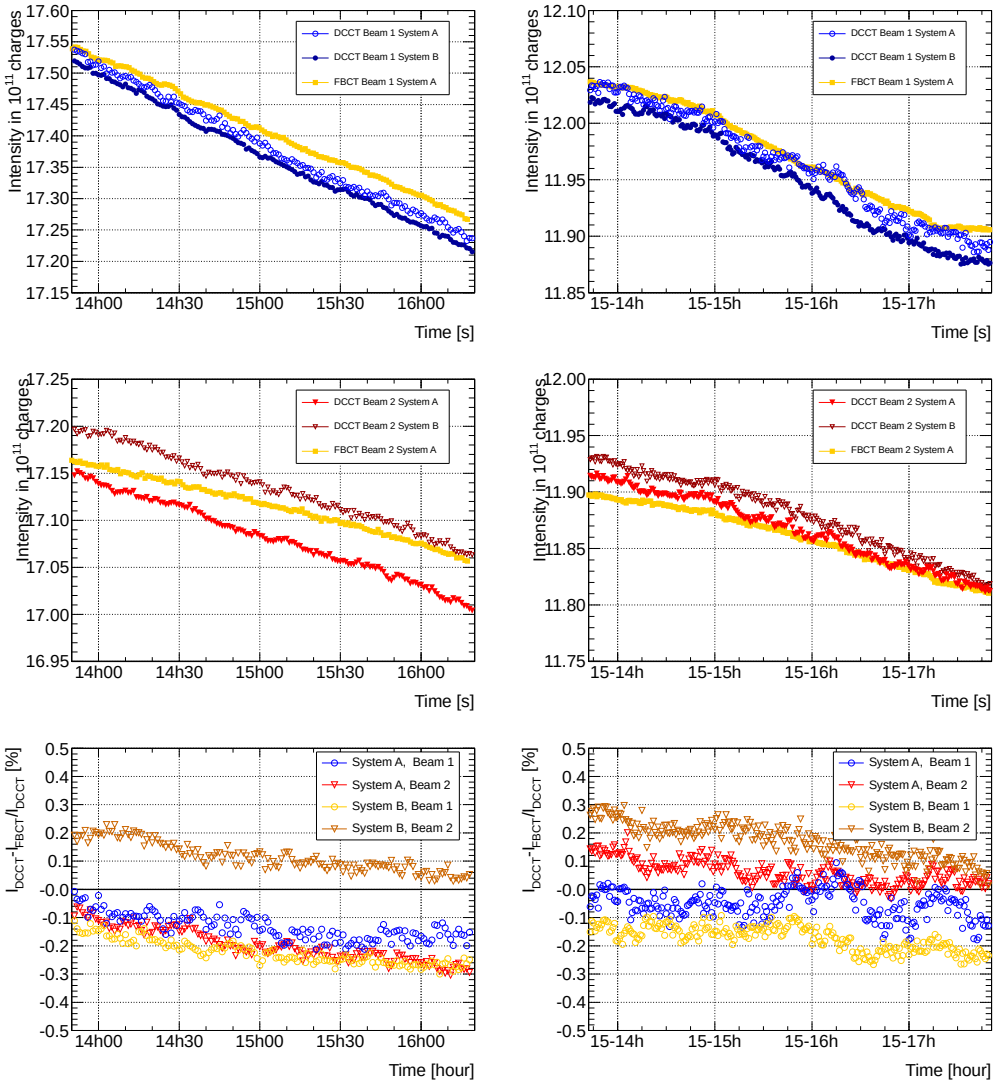

Figure 2: Comparison of the FBCT summed signals (yellow squares) and DCCT offset-corrected intensities in 10^{11} elementary charges (top and middle graphs) and as relative deviations (bottom graphs). Beam1 system A: open blue circles. Beam2 system A: solid red triangles. Beam1 system B: solid blue circles. Beam2 system B: open red triangles. Left graphs: fill 1386. Right graphs: fill 1422.

Note that work is ongoing to analyse the cross section normalizations obtained for the different colliding bunch pairs. This should allow one to better understand the response of the BPTX and FBCT systems and considerably reduce the systematic uncertainty associated with the relative bunch signals.

3.3 Ghost charge and satellite bunches

As for the April-May 2010 measurements, selected data rates from the experiments were used to constrain or measure the ghost charge and satellite bunches [3].

As in the previous note, the LHC convention is used for the coordinate system, i.e. $z = 0$ at the nominal IP, $z > 0$ in the clockwise direction ('left' and 'right' of an IP refer to $z < 0$ and $z > 0$).

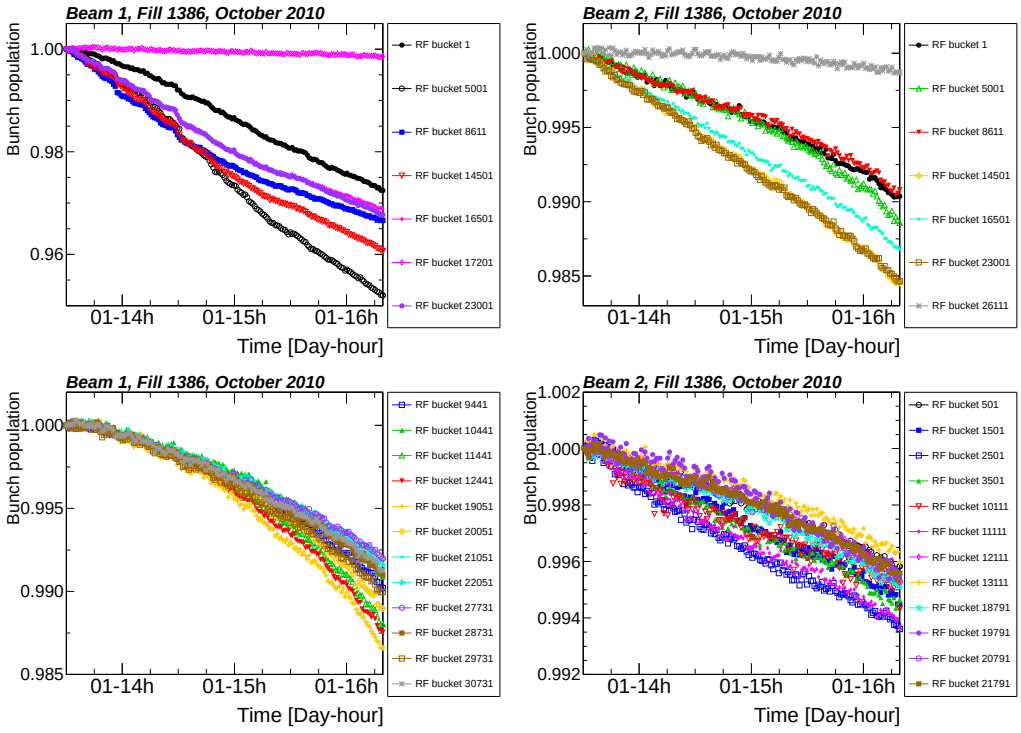

Figure 3: Bunch populations from the FBCT signals as a function of time for fill 1386. Left: Beam1. Right: Beam2. FBCT signals are each normalized to their first value. The top graphs show the population of the bunches colliding in IP1/5 and IP2. The bottom graphs show the population of the bunches colliding in IP8.

3.3.1 Ghost charge from beam-gas interactions

Interaction events were triggered in LHCb by a dedicated beam-gas trigger. The relevant hardware trigger (level-0) used two different channels for Beam1-gas and Beam2-gas interactions. For the Beam1-gas trigger, events were selected with a Calorimeter transverse energy sum larger than 5 GeV and a Pile-Up System multiplicity lower than 30. For the Beam2-gas trigger, events were selected with a transverse energy sum smaller than 1 GeV and a Pile-Up System multiplicity larger than 9. The trigger was enabled in all e-e, b-e and e-b crossings (we remind here that 'e' stands for a nominally empty 25 ns slot, and 'b' for a nominally filled 25 ns slot). The High Level Trigger selected events on a simple proto-vertexing algorithm, which looks for accumulation of tracks around a bin on the z axis.

In the offline analysis, a minimum number of 5 tracks per vertex was requested and a vertex position within $|z_{\rm vtx}| < 1.5$ m from the nominal IP. It was also required that the x and y positions of the vertex were within 2 mm from the average beam axis. The events are classified as 'forward', 'backward' or 'mixed' as explained in reference [3]. No pile-up correction was applied (this effect is small since the mean number of primary vertices per events with at least one primary vertex is in the range 1.04 to 1.08 for non b-b crossings).

Figures 6 and 7 show the distribution of forward, backward and mixed events in e-e crossings for fill 1386 and 1422. Figures 8 and 9 show the x-z distribution of reconstructed vertices of forward, backward and mixed type in e-e crossings for fill 1386 and 1422. All events passing the selection cuts are contained in the figures.

Table 10 summarizes the number of beam-gas events measured by LHCb during the two van der Meer scan fills. All recorded b-e (e-b) events were of forward (backward) type. Here, "near-bunch" stands for all slots that are $\pm 1 \ldots 3$ slots away from a nominally filled bunch slot. The subsets of events summed over these slots are given in brackets. The resulting ghost fractions are shown in table 11.

It is relevant to point out that this method of ghost charge determination has an intrinsic time granularity of 25 ns. The response to ghost charge in intermediate RF buckets, e.g. satellite bunches at ± 5 ns from a

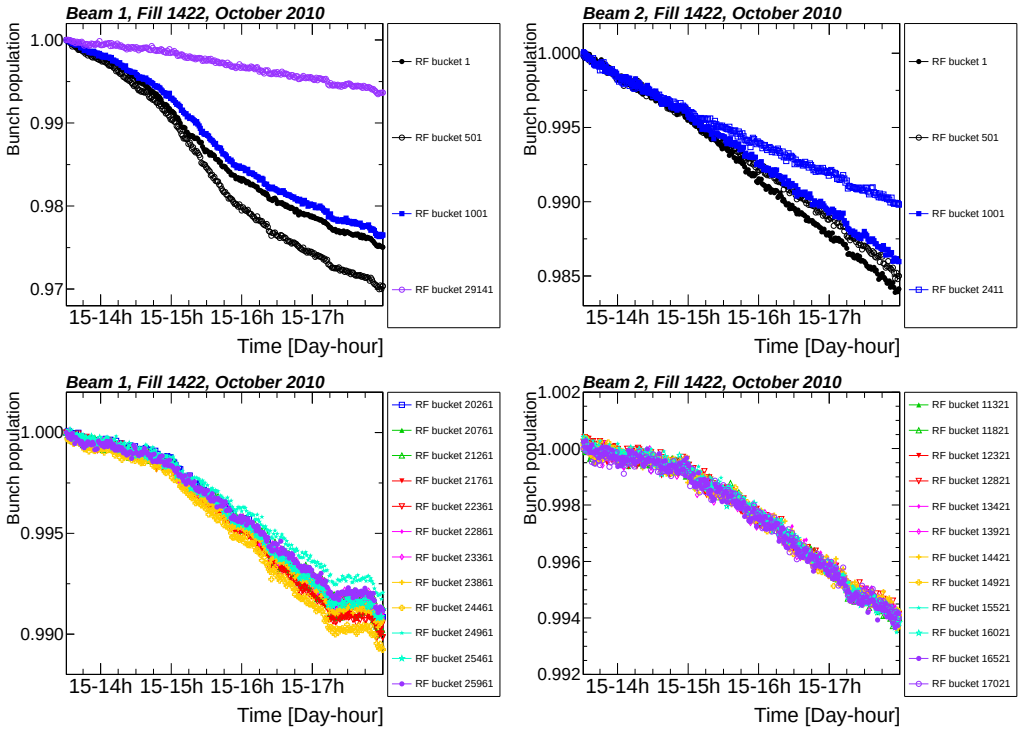

Figure 4: Bunch populations from the FBCT signals as a function of time for fill 1422. Left: Beam1. Right: Beam2. FBCT signals are each normalized to their first value. The top graphs show the population of the bunches colliding in IP1/5 and IP2. The bottom graphs show the population of the bunches colliding in IP8.

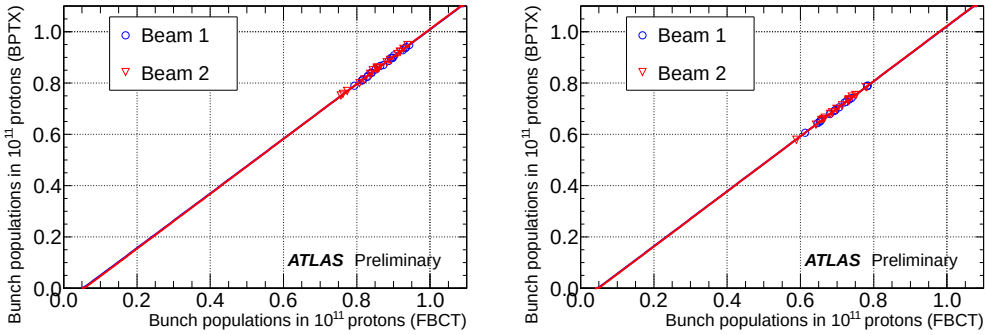

Figure 5: Bunch populations from the ATLAS BPTX versus the bunch populations from the FBCT signals, averaged over the full scan periods of each fill. Left: fill 1386. Right: fill 1422. Blue circles: Beam1. Red circles: Beam2. The summed populations of each set within a given fill was normalized to the same total current from the DCCT. The lines are the results of a fit for each beam and fill (see text).

nominal bunch slot, remains to be understood. The main systematic uncertainty will come from a possible trigger inefficiency as a function of the beam-gas event arrival time relative to the 25 ns slot center. Data in special configurations were taken during the October scan fills and analysis of this effect is under way. Trigger inefficiency can only cause an underestimation of the ghost charge (less beam-gas rate measured). A conservative estimate is to assume an average trigger efficiency of 75% uncertainty over the 25 ns slot and assign a 50% uncertainty on the resulting ghost charge[†]. This results in a ghost fraction of $0.27 \pm 0.13\%$ (Beam1) and $0.48 \pm 0.24\%$ (Beam2) for fill 1422 and $0.07 \pm 0.03\%$ (for each beam) for fill 1386. The

[†]A recent LHCb analysis (not detailed here) indicates that the actual trigger efficiencies averaged over a 25 ns slot are 85%, well within the given uncertainties.

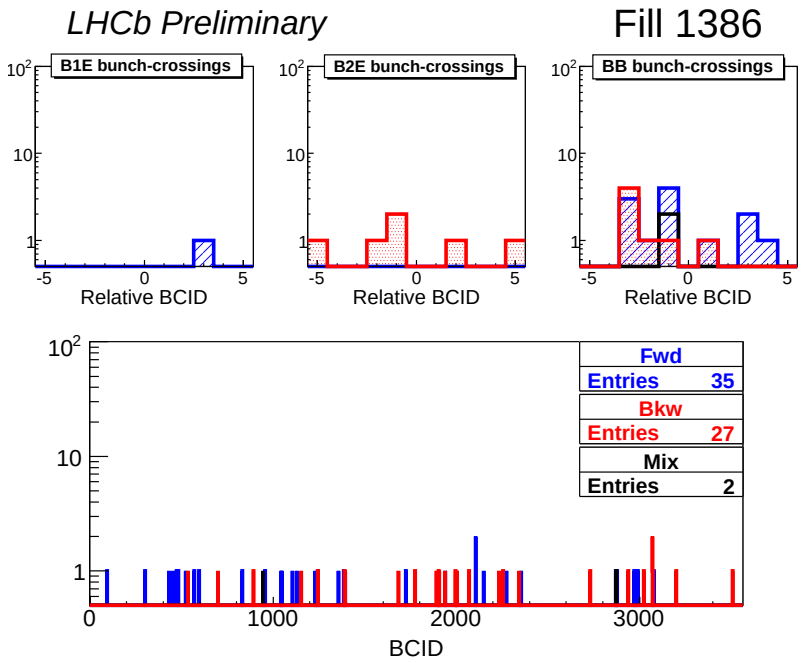

Figure 6: Number of forward (blue, hatched), backward (red, dotted) and mixed (black, empty) events as a function of Bunch Crossing ID for e-e crossings in fill 1386. BCIDs are counted modulo 3564. The top graphs show a zoom around the nominally filled bunches, grouped in three crossing types (the *x* axis is the BCID relative to the BCID of the nominally filled bunch). From left to right: b-e, e-b and b-b crossing types.

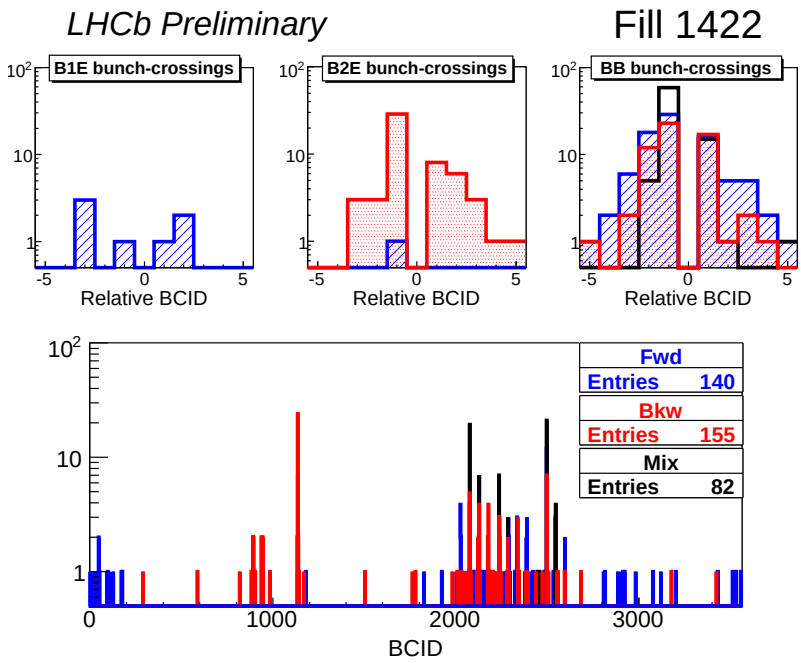

Figure 7: Number of forward (blue, hatched), backward (red, dotted) and mixed (black, empty) events as a function of Bunch Crossing ID for e-e crossings in fill 1422. BCIDs are counted modulo 3564. The top graphs show a zoom around the nominally filled bunches, grouped in three crossing types. From left to right: b-e, e-b and b-b crossing types.

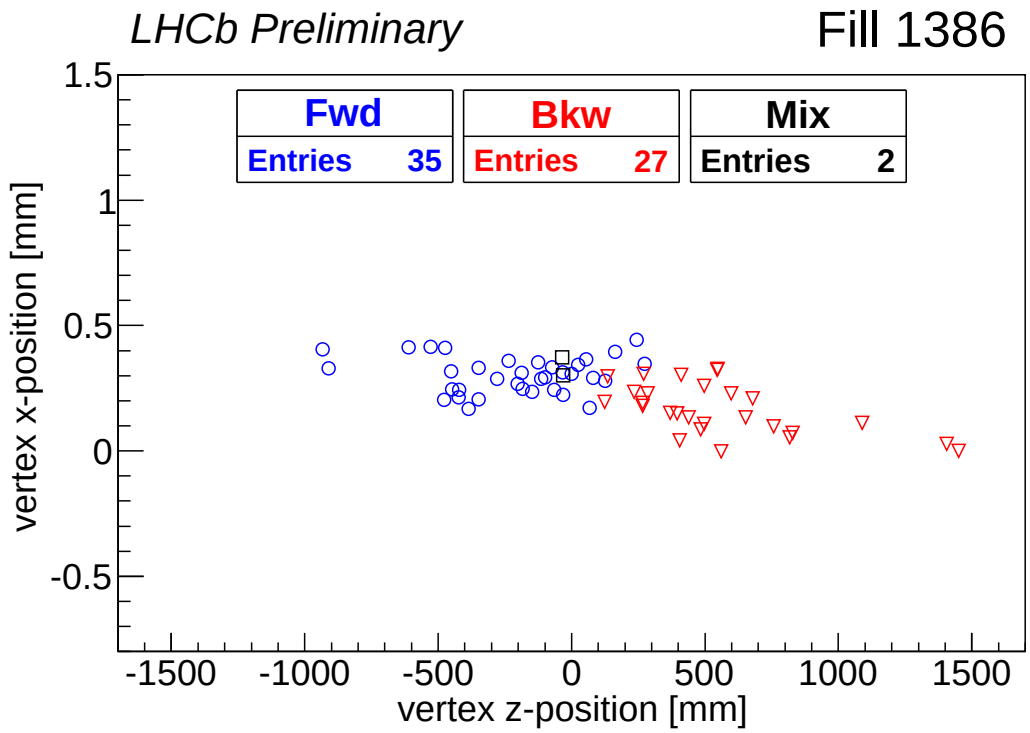

Figure 8: Distribution of reconstructed vertices in e-e crossings in the *x-z* plane for fill 1386: forward events (blue circles), backward events (red triangles), mixed events (black squares).

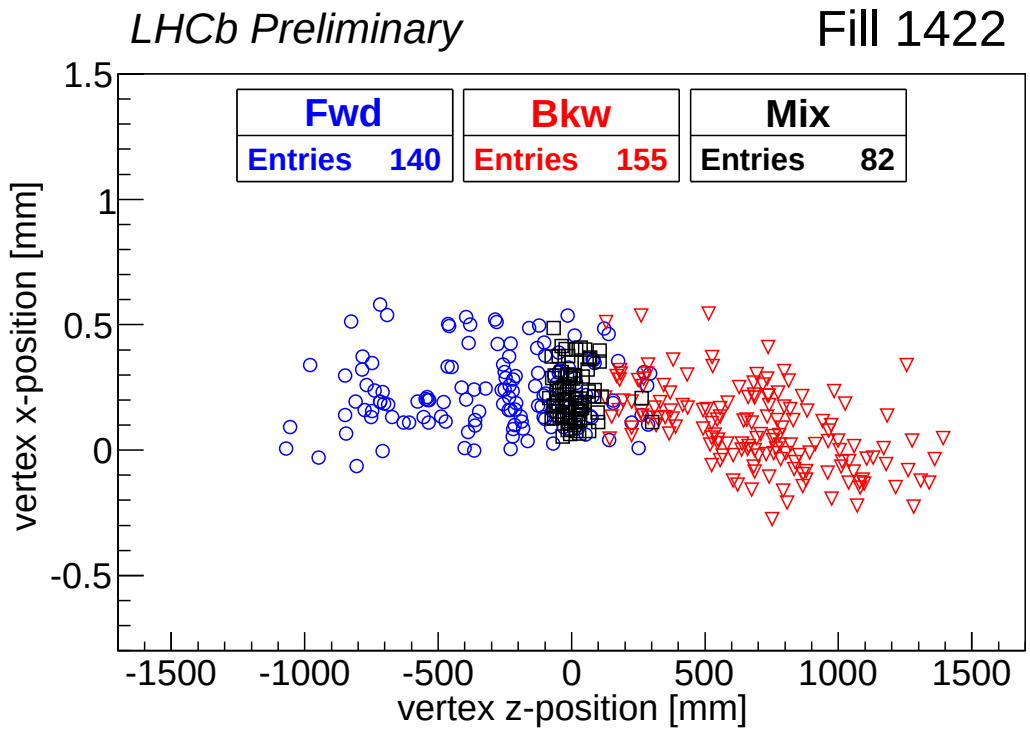

Figure 9: Distribution of reconstructed vertices in e-e crossings in the *x-z* plane for fill 1422: forward events (blue circles), backward events (red triangles), mixed events (black squares).

Fill number	Events in b-e	Events in e-b	Events in e-e (near-bunch) Forward		Backward		Mixed	
1386	26142	18243	35	(12)	27	(11)	2	(2)
1422	16228	10813	140	(87)	155	(109)	82	(80)

Table 10: Beam-gas events measured by LHCb in fills 1386 and 1422. All recorded b-e (e-b) events were of forward (backward) type. Here, "near-bunch" stands for all slots that are $\pm 1 \ldots 3$ slots away from a nominally filled bunch slot. The subsets of events summed over these slots are given in brackets.

Fill number		Beam1 ghost fraction $f_{\text{ghost},1} \cdot 10^2$ all slots	(near-bunch slots)	Beam2 ghost fraction $f_{\text{ghost},2} \cdot 10^2$ all slots	(near-bunch slots)
1386	raw values	0.05 ± 0.02	(0.02 ± 0.00)	0.05 ± 0.01	(0.02 ± 0.01)
	final values	0.07 ± 0.03		0.07 ± 0.03	
1422	raw values	0.20 ± 0.02	(0.12 ± 0.01)	0.36 ± 0.03	(0.25 ± 0.02)
	final values	0.27 ± 0.13		0.48 ± 0.24	

Table 11: Results for the ghost fraction (in percent), as extracted from LHCb beam-gas interaction data, before correction for a possible trigger inefficiency. Here, "near-bunch" stands for all slots that are $\pm 1 \ldots 3$ slots away from a nominally filled bunch slot. The ghost fractions concentrated in these slots are given in brackets. For the raw values, only statistical uncertainties are shown. The final values include an estimate of the sytematic uncertainties $\Delta f_{\text{ghost},j}$ (as explained in the text).

uncertainty, $\Delta f_{\text{ghost},j}$, is largely dominated by the trigger inefficiency uncertainty which is given here as an envelope bound. Strictly speaking, the ghost charge cannot be smaller than zero (by definition) and the error treatment should be done accordingly. However, given the smallnesss of the uncertainty, a treatment similar to what was done in reference [3] for the other bunch population uncertainties is used here: we transform the uncertainty into a 68% (Gaussian) CL for use in the bunch population product uncertainties, assuming the contributions from the two beams are uncorrelated, while they are assumed correlated from fill to fill.

3.3.2 Satellite bunch populations from timing and vertexing

All experiments also analyzed the pp interactions within a nominal b-b crossing that originated from possible satellite bunches, as explained in reference [3].

An important difference in the October scans was the presence of a net crossing half-angle ϕ in all IPs. In this configuration, a satellite bunch offset by Δt with respect to a nominal bunch ($\Delta t = 2.5, 5.0, 7.5 \ldots$ ns) will collide with the counter-rotating nominal bunch at a distance $z = c\Delta t/2$ from the IP, and with a relative transverse separation, in the crossing-angle plane, given by $d = 2z\tan\phi$. To estimate the satellite population, relative to a nominally filled bucket, from the rate of collisions at $z \neq 0$, corrections must be applied to take into account the luminosity reduction (compared to collisions at the nominal IP) associated with two distinct effects.

First, in the vicinity of the IP the β-function of each beam varies as

$$\beta(z) = \beta^* \cdot \left(1 + \left(\frac{z}{\beta^*}\right)^2\right) \tag{3}$$

in both the horizontal and the vertical plane, reflecting the angular divergence of the beam away from the focal point. This *hourglass effect* induces an increase in the transverse sizes (σ_{ix}, σ_{iy}) of beams $i = 1,2$:

$$\sigma_{iw}(z) = \sigma_{iw}(0) \cdot \sqrt{1 + \left(\frac{z}{\beta^*}\right)^2} \qquad (i = 1,2;\ w = x,y)\ . \tag{4}$$

The luminosity is inversely proportional to the convolved beam sizes $\Sigma_x(z)$ and $\Sigma_y(z)$. With a non-zero crossing angle in one plane, say the *x*-*z* plane, these are given by

$$\begin{aligned} \Sigma_x(z) &= \sqrt{2\,\sigma_x^2(z)\cos^2\phi + 2\,\sigma_z^2\sin^2\phi} \\ \Sigma_y(z) &= \sqrt{2}\,\sigma_y(z)\ . \end{aligned} \tag{5}$$

where we defined $2\,\sigma_u^2(z) = \sigma_{1u}^2(z) + \sigma_{2u}^2(z)$ for $u = x$, y and z. Using equation (4), the z-dependence of the convolved beam sizes is given by

$$\begin{aligned} \Sigma_x^2(z) &= \Sigma_x^2(0) + 2\,\sigma_x^2(0)\cdot\left(\frac{z}{\beta^*}\right)^2\cos^2\phi \\ &\approx \Sigma_x^2(0)\cdot\left(1+\left(\frac{z}{\beta^*}\right)^2\right) \qquad \text{if } \ \sigma_z\tan\phi \ll \sigma_x(z) \\ \Sigma_y^2(z) &= \Sigma_y^2(0)\cdot\left(1+\left(\frac{z}{\beta^*}\right)^2\right) \end{aligned} \tag{6}$$

where $\Sigma_x(0)$ and $\Sigma_y(0)$ are the effective widths directly measured during the van der Meer scan along the *x* and *y* axes. The corresponding decrease in luminosity is given by

$$\frac{L_{\text{hourglass}}(z)}{L(0)} = \frac{\Sigma_x(0)\,\Sigma_y(0)}{\Sigma_x(z)\,\Sigma_y(z)} \approx \left(1+\left(\frac{z}{\beta^*}\right)^2\right)^{-1} \tag{7}$$

where the last approximation is valid in the case $\sigma_z\tan\phi \ll \sigma_x(z)$. For $z = 75$ cm and $\beta^* = 350$ cm this correction factor amounts to approximately 0.956.

Next, the transverse separation d further reduces the luminosity by

$$\frac{L_{\text{d+hourglass}}(z)}{L_{\text{hourglass}}(z)} = e^{-\frac{d^2}{2\Sigma_w^2(z)}}\ . \tag{8}$$

For $z = 75$ cm, $\beta^* = 350$ cm, $d = 150\,\mu$m and $\Sigma_w = 80\,\mu$m, the correction factor given by equation (8) amounts to 0.186.

The correction factor r of the interaction rate, for two bunches colliding at z with a transverse separation d and taking into account the hourglass effect, is then given by

$$r = \frac{L_{\text{d+hourglass}}(z)}{L(0)} = e^{-\frac{d^2}{2\Sigma_x^2(z)}}\,\frac{\Sigma_x(0)\,\Sigma_y(0)}{\Sigma_x(z)\,\Sigma_y(z)}\ . \tag{9}$$

The above formalism is valid under the assumption that $\sigma_z \ll \beta^*$, i.e. that the transverse beam-size variation remains negligible on the scale of the bunch length. More complete formulas can be found in reference [5].

Experiment	β^*	ϕ	$\Sigma_w(0)$	$r(z = 37.5\text{ cm})$	$r(z = 75\text{ cm})$
ATLAS	3.5 ± 0.35 m	$100 \pm 10\,\mu$rad	$80 \pm 1\ \mu$m	$0.625^{-0.037}_{+0.041}$	$0.178^{-0.052}_{+0.065}$
CMS	3.5 ± 0.35 m	$100 \pm 10\,\mu$rad	$80 \pm 2\ \mu$m	-	$0.178^{-0.055}_{+0.069}$

Table 12: Summary of the luminosity correction factors used by the ATLAS and CMS experiments. The crossing plane is in the *w*-*z* plane, with $w = x, y$ depending on the IP.

The summary of the luminosity correction factors used by the ATLAS and CMS experiments are summarized in table 12. For these two experiments the bunch pairing is identical and satellite fractions can be directly compared.

3.3.2.1 CMS timing analysis

The charge contained in the satellite bunches, which precede or trail the main bunch by 5 to 10 ns, was estimated by searching for energy deposits in the CMS endcap calorimeters whose timing measurements are 5 ns earlier or later than those arising from collisions of the main bunches in each beam.

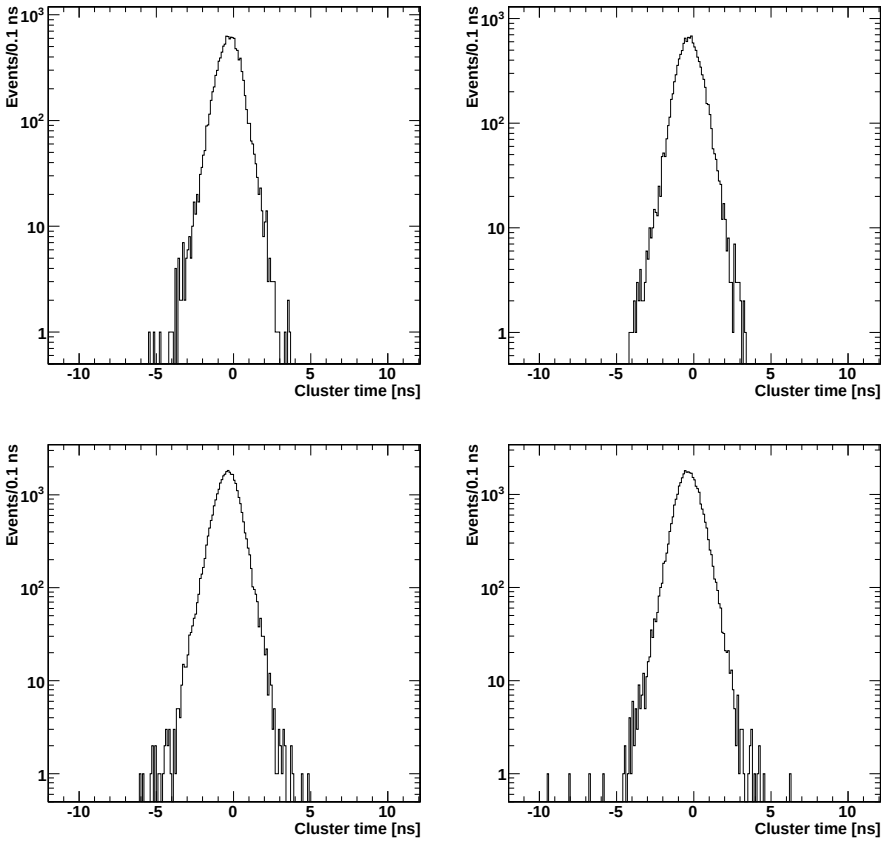

Figure 10: The timing distribution of clusters observed in EEP (left) and EEM (right) at CMS for LHC fills 1386 (top) and 1422 (bottom).

When one of these satellite bunches collides with the main bunch of the other beam, the resulting collisions are displaced along the z-axis and shifted in time. For example, a satellite bunch trailing the main bunch in Beam1 by 5 ns will collide with the main bunch of Beam2 at $z = -75$ cm, 2.5 ns after the collision of the two main bunches. The particles from this collision will be delayed by 5 ns in a detector on the $+z$ side, since the time of flight of these particles takes 2.5 ns more with respect to a nominal in-time collision at the interaction point. In a detector on the $-z$ side, however, the particles will appear in time, since the time of flight is 2.5 ns less, cancelling the collision time effect. By using detectors on both sides of the interaction point, signals from both leading and trailing bunches from each of the two beams can be seen.

To search for such signatures of displaced times, the electromagnetic calorimeter endcap detectors, EEP and EEM, which are placed on the left and right sides of IP5, have been used. Electromagnetic energy deposits in multiple crystals were reconstructed into clusters, with the seeding crystal required to have energy of more than 4 GeV. The time resolution for crystals above this energy is less than 1 ns. The data analyzed were taken with zero bias triggers in the same runs as the van der Meer scans, but before the scans began. It was not possible to look for evidence of satellites during the scan itself due to lack of statistics. The efficiency for the collisions to have such energy deposits in either EEP or EEM is estimated to be about 10%.

Figure 10 shows the reconstructed time of EE clusters relative to that expected for in-time collisions at the interaction point for LHC fills 1386 and 1422. The large peak centered around 0 ns is due to collisions between the main bunches in each beam. The offset from zero (about -0.3.ns) is due to an overall shift in

Fill	$\mathcal{S}_{+5\text{ns},0} \cdot 10^3$	$\mathcal{S}_{0,-5\text{ns}} \cdot 10^3$	$\mathcal{S}_{-75\text{cm}} \cdot 10^3$	$\mathcal{S}_{-5\text{ns},0} \cdot 10^3$	$\mathcal{S}_{0,+5\text{ns}} \cdot 10^3$	$\mathcal{S}_{+75\text{cm}} \cdot 10^3$
1386	< 0.94	< 6.97	< 7.87	< 3.69	< 2.87	< 6.03
1422	< 2.03	< 3.04	< 4.82	< 1.00	< 1.90	< 2.69

Table 13: CMS upper limits results (at 95% CL) for the ± 5 ns (trailing/leading) satellite bunch population relative to the main bunch. The $\mathcal{S}_{\pm 75\text{cm}}$ columns combine the limits of the two preceding columns.

the timing calibration. No peaking structure is visible at -5.3 ns or 4.7 ns, 5 ns away from the main peak near $t = 0$ ns, indicating that the fraction of protons in any satellite bunches is small. The shape of the tails of the main peak which can extend to the signal area were studied by using higher statistics data taken with different trigger conditions. This indicates that the few events observed in the signal region are consistent with what is expected from the tails of the main peak. However, no reliable estimates of the background contributions in each tail area could be made due to the differences in the running conditions. As a result, all events which fall in the ± 1 ns window centered around -5.3 ns, or 4.7 ns, were attributed to possible signal and used to set upper limits. These limits were compared to the number of events in the main peak, yielding the ratios $\mathcal{S}_{\pm 5\text{ns},0}$ and $\mathcal{S}_{0,\pm 5\text{ns}}$. The rate was multiplied by 5.62 to correct for the reduction in the luminosity for the satellite bunches due to the combined effect of the hourglass effect and of the finite separation in the positions of the two beams arising from the full crossing angle (about 200 μrad), which is significant compared to the convolved beam size ($\Sigma_x \approx 80\,\mu$m) at that location.

In addition, the acceptance of the endcap detectors changes when the collision point is displaced. Evaluating the change in acceptance using in one case the barrel detector and in the other case a smooth extrapolation, corrections of 1.205 for collisions occurring closer to the endcap and 0.608 for collisions farther from the endcap were determined. The amplitude of a reconstructed hit late in time is underestimated and could fail selection, so a correction from the known bias was applied. Finally, particles emerging from the collision could hit either endcap, so one must multiply by a factor of 2.

The upper limits of the ratios at 95% confidence level are presented in Table 13. The last two columns were calculated by combining the corresponding two columns in the table which arise from vertices at $z = \pm 75$ cm.

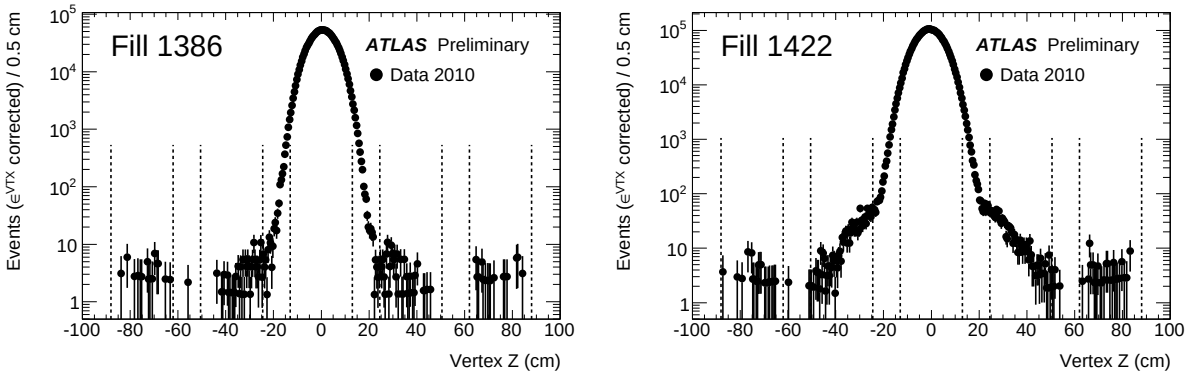

Figure 11: ATLAS primary vertex distribution as a function of z_{vtx} for fills 1386 (left) and 1422 (right), after correcting for vertex reconstruction efficiency.

3.3.2.2 ATLAS vertexing analysis

Figure 11 shows the ATLAS primary vertex distribution for fill 1386 and 1422, after correcting for the vertex reconstruction efficiency. The central peak is due to interactions from the colliding main bunches. Two additional peaks are clearly visible at $z \approx \pm 75$ cm and are attributed to interactions from the crossing of the main bunches with a satellite bunch displaced by ± 5 ns relative to the main bunch. Note that this method alone cannot discriminate between a trailing satellite in Beam2 colliding with the main bunch of

Beam1 and a leading satellite in Beam1 colliding with the main bunch of Beam2 (or vice versa): both give rise to displaced collisions at $z \approx +75$ cm (respectively, -75 cm).

The reconstruction efficiency of the vertexing algorithm was estimated from Monte Carlo simulation and is shown in figure 12 as a function of the z vertex position.

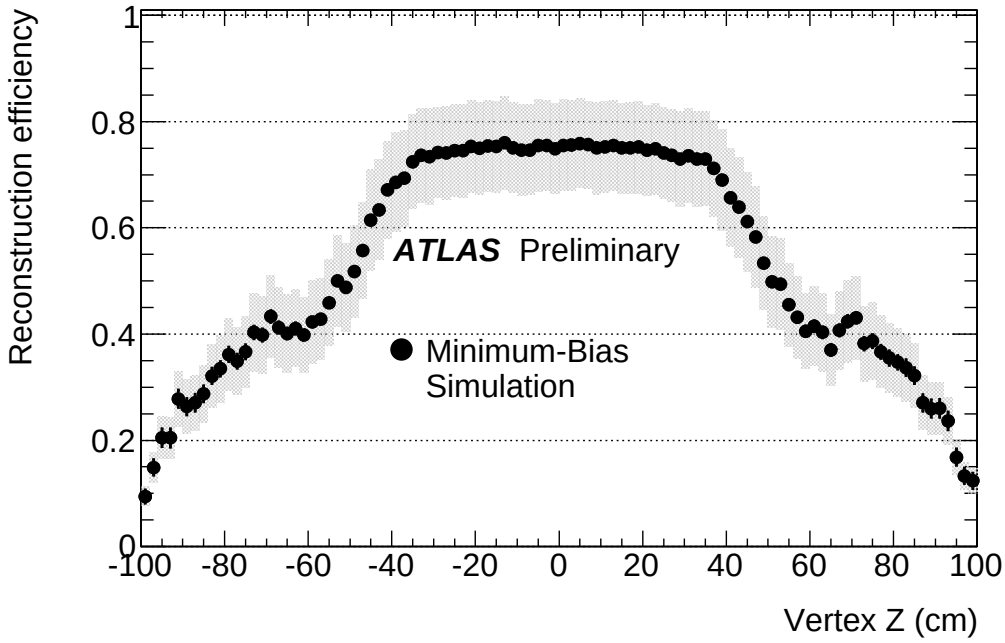

Figure 12: ATLAS primary vertex reconstruction efficiency for the loose vertex reconstruction algorithm used in this work, shown as a function of z_{vtx}, as obtained from a Monte-Carlo simulation.

The ATLAS results are summarized in table 14 which gives the satellite population as a fraction of the average main bunch population. Note that, to simplify the limit setting procedure, the systematic uncertainties on the reduction factor have been "symmetrized" in the final numbers. To be conservative, the largest of the $\pm$ uncertainties was used. The details of the ATLAS satellite analysis from vertexing can be found in reference [6].

Fill	$\mathcal{S}_{+37.5\text{cm}}$ (10^{-3})	$\mathcal{S}_{-37.5\text{cm}}$ (10^{-3})	$\mathcal{S}_{+75\text{cm}}$ (10^{-3})	$\mathcal{S}_{-75\text{cm}}$ (10^{-3})
1386	< 0.16	< 0.15	< 0.34	< 0.35
1422	< 0.56	< 0.52	< 0.31	< 0.22

Fill	$\mathcal{S}_{+75\text{cm}}$ (10^{-3})	$\mathcal{S}_{-75\text{cm}}$ (10^{-3})
1386	0.205 ± 0.085	0.207 ± 0.085
1422	0.185 ± 0.076	0.133 ± 0.055

Table 14: ATLAS results on satellite fractions from vertexing. Left: 95% CL upper limits on the satellite current ratio $\mathcal{S}_z$. $\mathcal{S}_{\pm 37.5\text{cm}}$ represents the rate of satellite collisions around $z \approx \pm 37.5$ cm, while $\mathcal{S}_{\pm 75\text{cm}}$ represents the one from satellite collisions around $z \approx \pm 75$ cm. The quoted limits include statistical and systematic uncertainties (see text for details). Right: Measured current ratio for satellite collisions around $z \approx \pm 75$ cm in the hypothesis of no background.

3.3.2.3 CMS vertexing analysis

The displaced vertex reconstruction method was applied by CMS, as described in [3]. Figure 13 shows the raw vertex distribution.

To obtain the satellite fractions, the rates were corrected for the hourglass effect and the separation at the nominal location of the collisions. The reconstruction efficiency was estimated from Monte-Carlo simulation, as in reference [3]. No pile-up correction was applied (the correction is expected to be $< 7\%$). The

satellite fractions are listed in table 15. The uncertainties quoted in this table do not include the ones from the correction factor r given in table 12.

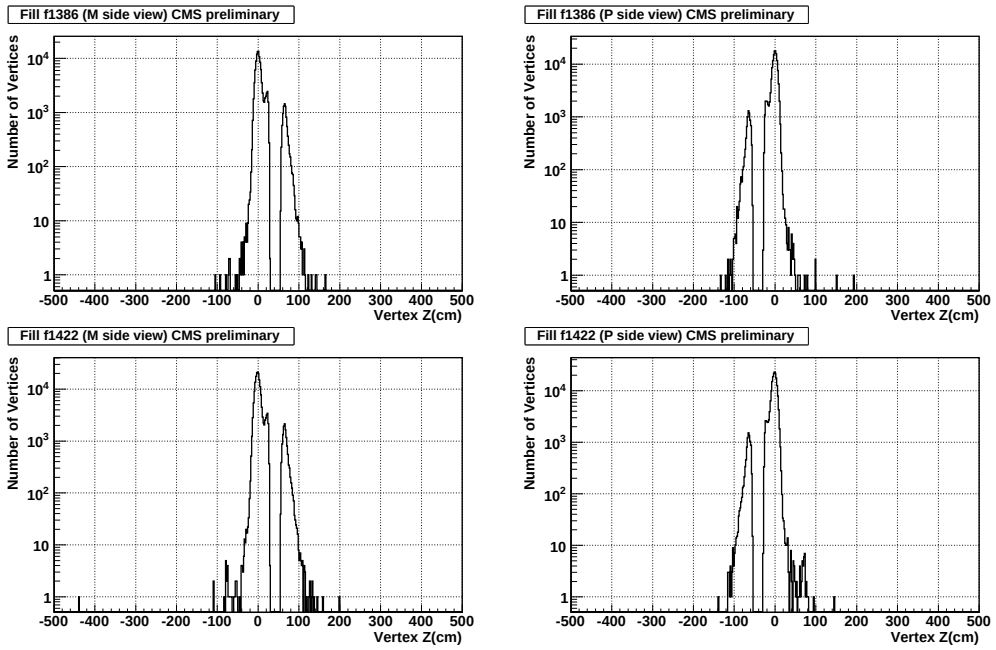

Figure 13: CMS vertex distribution as a function of z for fill 1386 and 1422, using the M side (left graph) or the P side (right graph) of the tracker, before correcting for vertex reconstruction efficiency, hourglass and beam separation.

Satellite bunch fractions $\mathcal{S}_z \cdot 10^3$ at different z.				
$z =$	-150	-75	+75	+150 cm
Fill 1386	< 5.9	0.34 ± 0.07	0.08 ± 0.06	< 15.2
Fill 1422	< 5.2	0.58 ± 0.12	0.87 ± 0.24	< 11.0

Table 15: Satellite bunch fractions from CMS vertexing of the displaced collisions relative to the IP for fill 1386 and 1422. The uncertainties do not include those on the reduction factor given in table 12. Upper limits are at 95% confidence level.

3.3.2.4 ALICE timing analysis

The ALICE experiment performed a timing analysis of the events during the van der Meer scans in IP2. The most favorable conditions for the observation of satellite collisions in ALICE occurred during the vertical van der Meer scan. When the beams were moved one across the other, the separation between the main bunch of one beam and the satellites of the other beam was reduced. For collisions at $z = \pm 75$ cm, such separation amounted to 250 $\mu rad \times 2 \times 75$ cm$=$ 375 μm. The maximum beam separation reached in IP2 during the scan was 300 μm. In these conditions, main-satellite collisions occurred at $z = \pm 75$ cm with a separation of 75 μm.

Observation of longitudinally displaced collisions for the October scan was performed in ALICE with the V0 detector [7], which consists of two scintillator arrays located at $z = -340$ cm (V0A) and $z = 90$ cm (V0C) The V0 time resolution is better than 1 ns. The expected arrival time difference $t_A - t_C$ between V0A and V0C is 3.3 ns for collisions at $z = -75$ cm and it is 13.3 ns for collisions at $z = 75$ cm and 8.3 ns for collisions at $z = 0$.

Figure 14 shows the V0 arrival time difference as a function of the beam separation during the vertical van der Meer scan, for events originating from collisions of the main bunch of Beam1[‡]. As the separation in-

[‡]This selection was performed via a cut on the sum of arrival times.

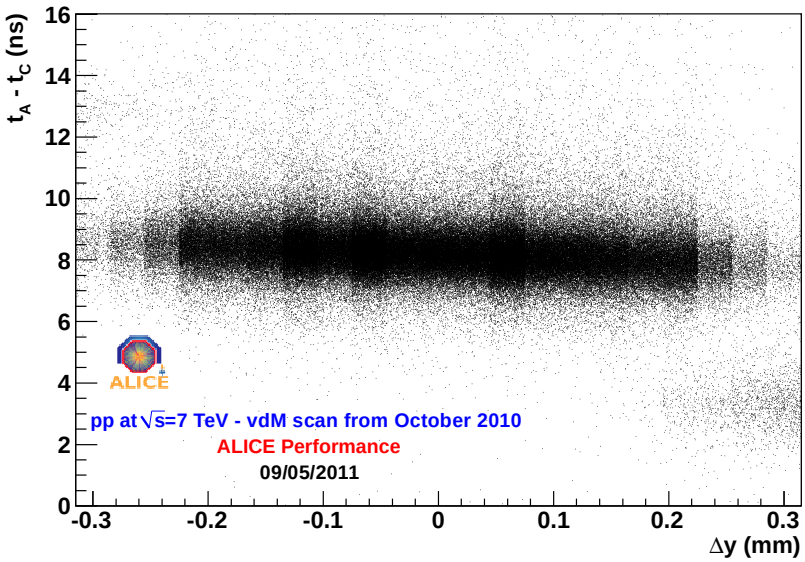

Figure 14: Distribution of the V0 arrival time difference $t_A - t_C$ versus the beam separation during the vertical van der Meer scan in IP2 (fill 1422).

creases, the number of events with time difference corresponding to collisions at $z = -75$ cm also increases. The effect is maximum when the separation is 300 μm. A similar effect, less important in magnitude, is also seen for collisions at $z = 75$ cm and a separation of 300 μm in the opposite direction. The same plot was produced for the collisions of the main bunch of Beam2, but no such effect was observed.

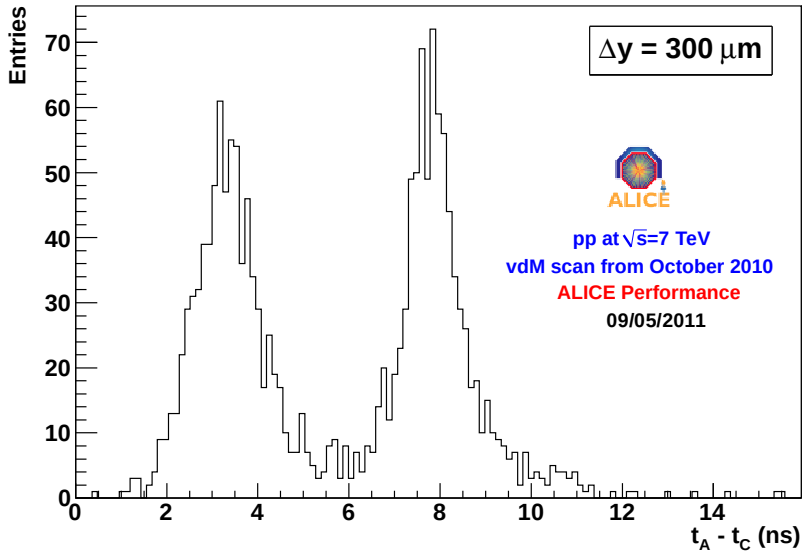

Figure 15: Distribution of the V0 arrival time difference $t_A - t_C$ during the vertical van der Meer scan in IP2 (fill 1422), at the beam separation of $\Delta y = 300$ μm.

Figure 15 shows the distribution of the V0 arrival time difference when the separation was 300 μm. Two peaks of similar magnitude are seen, showing that about 50% of the collisions at maximum separation originated from satellite bunches.

Three corrections are needed to estimate the satellite bunch population from the number of satellite collisions: beam separation, hourglass effect and trigger efficiency.

The beam separation correction is needed to take into account the fact that, when the main-to-main collisions occur at a 300 μm separation, the main-to-satellite collisions occur at 75 μm separation. Thus, the specific luminosity is higher for main-to-satellite collisions (by a factor $\simeq 10^2$). The ratio between the specific luminosities at the two separation values is obtained from the shape of the luminosity versus separation curve measured in the van der Meer scan itself [8].

A correction for the hourglass effect ($\simeq 4\%$) and a trigger efficiency correction ($\simeq 2\%$, obtained from simulation) for collisions at $z = \pm 75$ cm were also applied.

The satellite bunch populations obtained from this analysis are the following: $(0.6 \pm 0.2)\%$ of the main bunch for the leading satellite of Beam2 colliding with the main satellite of Beam1 at $z = -75$ cm; $(0.2 \pm 0.1)\%$ of the main bunch for the trailing satellite of Beam2 colliding with the main satellite of Beam1 at $z = 75$ cm. The same procedure did not lead to the observation of satellites in Beam1. The quoted errors have been obtained by varying the crossing angle by 10% with respect to the nominal value, by varying the method with which events in the main and satellite peaks are counted (Gaussian fit versus bin counting), by comparing the results obtained at 300 μm separation with those obtained and 270 μm and 240μm separation, and by comparing the results obtained in two different vertical scans in the same fill.

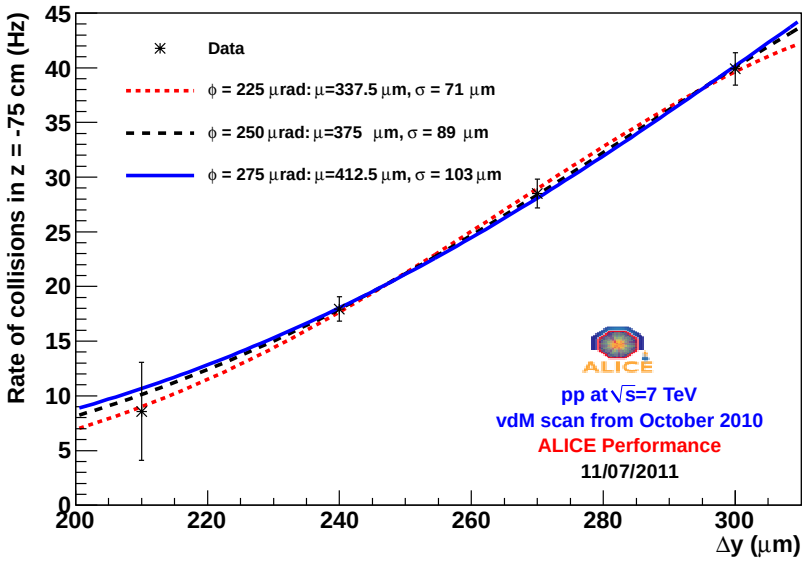

Figure 16: Rate of collisions at $z = -75$ cm (main bunch of Beam1 with satellite bunch of Beam2) as a function of the beam separation during the vertical van der Meer scan in IP2 (fill 1422). Gaussian fits for three different crossing angle hypotheses are also shown.

The measurement of the rate of satellite collisions versus the vertical beam separation in the van der Meer scan can be used to estimate the width of the satellite bunch. This was performed by fitting the data points with a Gaussian function whose mean value was fixed to the expected position of the head-on main-to-satellite collisions, i.e. 375 μm for a half crossing angle of 250 μrad. The fit result is shown in figure 16, together with those obtained by varying by 10% the value of the crossing angle (hence the position of the head-on main-to-satellite collisions). The fitted value for the scan width is $\sigma_{main-sat.} = (89 \pm 4)$ μm. This value is quite similar to the result obtained for the main-main collisions [8]: $\sigma_{main-main} \simeq 92$ μm, pointing to a similar width for the main and satellite bunches. However, such result strongly depends on the assumption that the crossing angle is close to the nominal value: the fitted width is about 20 μm (10 μm) smaller (larger) if one assumes a crossing angle smaller (larger) by 10% (figure 16).

4 Discussion and summary

In this note, the bunch population normalization for the October 2010 van der Meer scans was presented.

The analysis procedure was the same as for the April-May 2010 scans, as described in reference [3], except for a minor difference in the treatment of the ghost charge, which was no longer negligible. Owing to the fact that larger bunch populations and total beam populations were used in the October scans, the bunch population uncertainties were considerably reduced. The October uncertainties on the bunch populations are at the level of 3.1% (68% CL), dominated by the DCCT scale uncertainty and the FBCT relative populations uncertainties.

The satellite bunch analyses showed that the satellite bunches at ± 5 ns from the main (colliding) bunches were below the permil level for ATLAS and CMS (fills 1386 and 1422) and at the few permil level for ALICE (fill 1422), still negligible compared to other sources of uncertainties. As in the 2010 April-May fills, no sign of satellite bunches at ± 2.5 ns was found.

Most relevant to the extraction of a cross section from the luminosity calibration measurements is the bunch population product $P_{ij} = N_{i,1} N_{j,2}$ with $N_{i,1}$ the population of bunch i of Beam1 and $N_{j,2}$ the population of bunch j of Beam2. Table 16 summarizes the treatment of uncertainties $\sigma_{P_{ij}}$ of the population product for the extraction of the visible cross sections.

Final 68% CL uncertainty on any given bunch population product P_{ij}

$$\sigma_{P_{ij}} = \sqrt{(\sigma^{\text{baseline}}_{P_{ij}})^2 + (\sigma^{\text{ghost}}_{P_{ij}})^2 + (\sigma^{\text{scale}}_{P_{ij}})^2 + (\sigma^{\text{FBCT}}_{P_{ij}})^2}$$

Source of uncertainty	Contribution to uncertainty		Correlation between bunches	Correlation between fills
DCCT baseline	$\frac{\sigma^{\text{baseline}}_{P_{ij}}}{P_{ij}}$	$= 0.682 \cdot \sqrt{\left(\frac{\Delta N_{\text{tot},1}}{N_{\text{tot},1}}\right)^2 + \left(\frac{\Delta N_{\text{tot},2}}{N_{\text{tot},2}}\right)^2}$ $= 0.05\%$ (fill 1386), 0.07% (fill 1422)	full	none
Ghost charge	$\frac{\sigma^{\text{ghost}}_{P_{ij}}}{P_{ij}}$	$= 0.682 \cdot \sqrt{\left(\Delta f_{\text{ghost},1}\right)^2 + \left(\Delta f_{\text{ghost},2}\right)^2}$ $= 0.03\%$ (fill 1386), 0.19% (fill 1422)	full	full
DCCT scale	$\frac{\sigma^{\text{scale}}_{P_{ij}}}{P_{ij}}$	$= 0.682 \cdot 2 \cdot \frac{\Delta\alpha}{\alpha} = 2.7\%$	full	full
FBCT linearity	$\frac{\sigma^{\text{FBCT}}_{P_{ij}}}{P_{ij}}$	$= 0.682 \cdot \sqrt{\left(\frac{\Delta N_{i,1}}{N_{i,1}}\right)^2 + \left(\frac{\Delta N_{j,2}}{N_{j,2}}\right)^2} = 1.6\%$	full	none

Table 16: Summary of the treatment of uncertainties for the presented analysis. The contribution from the DCCT baseline is here negligible, but is shown for comparison to the April-May 2010 results [3].

Further improvements may still arise from a more detailed analysis of the per-bunch cross section normalization results. Ongoing studies of the DCCT scale and stability will hopefully lead also to a further reduction of the bunch poplulation normlization uncertainty to the benefit of future luminosity calibration experiments.

5 Acknowledgements

We would like to thank the CERN management and the LHC Collaborations for their support and encouragements to carry out this work.

References

[1] *"Luminosity Determination in pp Collisions at sqrt(s)=7 TeV Using the ATLAS Detector at the LHC"*, ATLAS Collaboration Collaboration, G. Aad *et al*., Eur.Phys.J. C71 (2011) 1630; *"Updated Luminosity Determination in pp Collisions at sqrt(s) = 7 TeV using the ATLAS Detector"*, ATLAS Collaboration, ATLAS-CONF-2011-011, 2011.

[2] See in Proceedings of the LHC Lumi Days (LHC Workshop on LHC Luminosity Calibration), 13-14 January 2011, CERN (Geneva, Switzerland), H. Burkhardt, M. Ferro-Luzzi, A. Macpherson and M. Mangano eds., CERN-Proceedings-2011-001, http://cdsweb.cern.ch/record/1347440?ln=en.

[3] *"LHC Bunch Current Normalisation for the April-May 2010 Luminosity Calibration Measurements"*, G. Anders *et al*. (BCNWG note1), CERN-ATS-Note-2011-004 PERF. http://cdsweb.cern.ch/record/1325370.

[4] *"Concept of Luminosity"*, W. Herr and B. Muratori, in CAS - CERN Accelerator School: Intermediate Course on Accelerator Physics, Zeuthen, Germany, 15 - 26 Sep 2003, pp.361-378. http://cdsweb.cern.ch/record/941318.

[5] *"Determination of the Absolute Luminosity at the LHC"*, S.M. White, CERN-THESIS-2010-139, LAL-10-154. http://cdsweb.cern.ch/record/1308187.

[6] *"Upper Limits on the Charge in Satellite Bunches for the October 2010 LHC Luminosity Calibration"*, The ATLAS collaboration, ATLAS-CONF-2011-049. http://cdsweb.cern.ch/record/1340989

[7] P. Cortese *et al*. (ALICE collaboration), ALICE-TDR-011 / CERN-LHCC-2004-025 (10 September 2004).

[8] K. Oyama *et al*. (ALICE collaboration), proceedings of the "LHC Lumi Days" workshop, CERN-Proceedings-2011-001.